Comparisons of Mixing Efficiency for a Strut Fuel Injector Obtained from Large-Eddy and Reynolds-Averaged Simulations, and Experiments

Tomasz G. Drozda,[†] Robert A. Baurle,[†] Cody R. Ground,[†] and Karen F. Cabell.[†]
NASA Langley Research Center, Hampton, VA 23681

ABSTRACT

Mixing efficiency is obtained for a strut fuel injector at hypervelocity flow conditions by using large-eddy simulations (LES), Reynolds-averaged simulations (RAS), and experiments. The injector and flow conditions have been previously investigated by using RAS and experiments as a part of the Enhanced Injection and Mixing Project (EIMP) at the NASA Langley Research Center (LaRC). Because the fidelity of LES is a strong function of the grid, the mixing efficiency is obtained on two grids, the coarser of which is a factor of two coarser in each of the three dimensions with respect to the fine grid. The RAS uses the two-equation linear eddy viscosity and diffusivity modeling of Menter. In RAS, the species diffusivity model exhibits a strong dependence on the turbulent Schmidt number, which is often adjusted until some metric of engineering interest, such as the mixing efficiency, matches the experimental data. In the absence of experimental data, scale-resolving simulations, such as LES, have been proposed as surrogates for experiments that could provide the data needed to "calibrate" the turbulent Schmidt number in the RAS models. This approach is followed because LES requires significantly more computational resources (CPU, data storage, and time) than RAS, making it prohibitive for use in many engineering applications and specifically for parameter exploration or optimization. Here we examine the mixing efficiency obtained from several RAS with different values of the turbulent Schmidt number, and compare the results with those obtained from the LES and experiments. In addition, the least squares fitting approach was used to demonstrate how to obtain an estimate for the turbulent Schmidt number from LES analytically. These estimates were then used together with prior knowledge about RAS model sensitivity to select a turbulence model that was expected to best match the LES data.

[†]Research Scientist, Hypersonic Airbreathing Propulsion Branch.

INTRODUCTION

Fuel injector design, leading to efficient fuel-air mixing, combustion, and flameholding, remains one of the key challenges in scramjet flowpath design. Attempts to improve the fuel-air mixing, while simultaneously reducing total pressure losses, have received a great deal of attention over the years.[1] The Enhanced Injection and Mixing Project (EIMP) being executed at the NASA Langley Research Center, represents an effort to achieve more rapid mixing at high speeds.[2] In the experiments, which are underway in the Arc-Heated Scramjet Test Facility (AHSTF), various fuel injection devices are being tested on an open flat plate located downstream of a Mach 6 facility nozzle, which emulates the combustor of a flight vehicle traveling at a Mach number of about 14 to 16. The experiments use nitric oxide (NO) planar (P) laser-induced fluorescence (LIF), or NO PLIF, for flow visualization. In-stream measurements of pitot pressure, total temperature, and gas composition are made with probes that can be traversed across any cross-stream plane downstream of the injectors. Mixing efficiency is computed from the experiments using a recently developed approach that relies on the in-stream measurements to estimate local mass flux distribution.[3] The tests are conducted at a reduced total temperature to allow for uncooled test hardware and use helium in order to focus on mixing and reduce the complexity and cost of the experiment. The mixing characteristics of the three baseline fuel injectors: strut, ramp and flushwall, have been extensively studied computationally.[4–10]

All previous studies performed Reynolds-averaged simulations (RAS), which are routinely used in the aerospace industry. Unfortunately, RAS, which attempts to model all the flow scales present in turbulent flows, have proven to be deficient in many challenging areas of interest to the aerospace community, e.g., high lift devices (smooth body separation), combusting flows (particularly lean or rich flames near extinction), unsteady flows (rotorcraft, aeroacoustics), and shock / boundary layer and shock / jet interactions. In many engineering applications, the limitations of the turbulence models are the pacing items preventing the use of RAS as a true predictive tool.[11]

Large-eddy simulation (LES) methods have the potential to reduce the modeling uncertainty inherent to RAS approaches because LES methods resolve the large scale turbulent structures while modeling only the smallest "subgrid" scales. However, the computational expense of LES at relevant Reynolds numbers is often not practical. Hybrid RAS/LES approaches[12,13] have emerged to address this issue, and have provided a rational path forward toward extending LES into practical settings. However, the computational expense required for hybrid RAS/LES is still high when compared to RAS. Moreover, the numerical algorithms required to partially resolve the turbulence scales must have low numerical dissipation properties with minimal dispersive errors, a feature typically not required of RAS solvers.

In the current work, mixing efficiency is obtained for a strut fuel injector using RAS, LES, and experiments. The RAS uses the two-equation linear eddy viscosity and diffusivity modeling of Menter.[14] In RAS, the species diffusivity model exhibits a strong dependence on the turbulent Schmidt number ($\mathrm{Sc_t}$), which is often adjusted until some metric of engineering interest, such as the mixing efficiency, matches the experimental data. In the absence of the experimental data, LES has been proposed as a surrogate for experiments, and could provide the data needed to "calibrate" the $\mathrm{Sc_t}$ in the RAS models. The current simulations were intended to assess the feasibility of LES to serve as such a surrogate. Two approaches are evaluated. The first approach uses the LES data in a conventional fashion, where the mixing efficiency obtained from the LES is directly compared to that from RAS for a range of $\mathrm{Sc_t}$ values varied from 0.1–1.0. The second approach uses a least-squares "best-fit" method to extract an approximate value of the $\mathrm{Sc_t}$ that should be used with a RAS gradient diffusion model. Any discrepancy found between these two methods could provide insight into RAS model-form uncertainty and reveal cases where the $\mathrm{Sc_t}$ is being tuned to reduce the model-form errors.

DEFINITION OF MIXING EFFICIENCY

For the current study, the one-dimensional mixing efficiency, η_m, based on stoichiometric proportions of fuel and air was chosen as the metric of interest. The mixing efficiency is defined in this work following Mao et al.:[15]

$$\eta_m = \frac{\int Y_R \rho u \, dA}{\int Y \rho u \, dA} \tag{1}$$

where Y is the fuel or oxidizer mass fraction depending on whether the global ER is less than or greater than 1, respectively. The quantity Y_R is defined as the amount of fuel or oxidizer that would react if complete reaction took place without further mixing, i.e.,

$$Y_R = \begin{cases} Y, & Y \leq Y_{st} \\ \frac{Y_{st}}{1-Y_{st}}(1-Y), & Y > Y_{st} \end{cases} \tag{2}$$

where Y_{st} is the stoichiometric value of fuel or oxidizer mass fraction. For cases with overall ER of one, either fuel or oxidizer can be used in place of Y. However, choosing the fuel has a minor benefit of clarifying the meaning of Eq. (2), which becomes

$$Y_R = \begin{cases} Y_f, & Y_f \leq Y_{f,st} \\ FAR_{st}\, Y_a, & Y_f > Y_{f,st} \end{cases} \tag{3}$$

where subscripts f and a denote fuel and air streams, respectively. The quantity FAR_{st} denotes the stoichiometric value of the fuel-to-air ratio and is equal to 0.0293 for hydrogen-air mixtures. From this equation, if the local value of the mass fraction of fuel is less than its stoichiometric value, then that amount is "counted" as fully mixed because there is a sufficient amount of air to potentially deplete all the fuel if reactions were allowed. However, when the local value of the fuel mass fraction is greater than its stoichiometric value, then the only part that could react is that which is in stoichiometric proportion to the local value of the mass fraction of the air. Therefore, only that portion is counted as being mixed in Eq. (1). The mixing efficiency formula in Eq. (1) can also be used to analyze mixing in reacting simulations; however, since fuel and oxidizer are consumed to make combustion products, care must be taken to use the elemental mass fractions of either fuel or oxidizer (i.e., mass fractions of all elements that originate in either fuel or oxidizer streams).

EXPERIMENTAL FACILITY, HARDWARE, AND DATA

EIMP experiments entail testing various fuel injection devices mounted on an open flat plate located downstream of a Mach 6 facility nozzle. The open flat plate is used because it facilitates optical access to the test region and simplifies experimentation. Figure 1 shows the cross section of the experimental apparatus mounted in the 4 ft diameter test cabin. Noted on the figure is the flat plate test bed platform with its leading edge positioned 2.5 inches below the top wall of the Mach 6 facility nozzle. The flow is from left to right. The flat plate is approximately 29 inches long tip-to-tail and 32 inches wide, and features an interface for mounting interchangeable injector blocks. The trailing edge of the injector block is located 8.87 inches downstream of the test bed plate leading edge. The injector blocks can accommodate a spanwise row of several injectors. The facility air flows over the injector bodies and mixes with the fuel simulant (helium) downstream of the injection plane. Also noted in Fig. 1 are the in-stream rake traverse system (used for pitot pressure, total temperature, and gas sampling probes), the jet stretchers, and the instrumentation shroud located on the upper side of the flat plate. The figure also shows the orientation of the experimental apparatus as installed in the AHSTF test cabin. In subsequent CFD simulations, the positive y-direction is oriented in the plate-normal direction, which in this figure is pointing toward the ground. Further details about the experimental setup and EIMP are presented in Cabell et al.[2] Current experiments focus on studying fuel injection and mixing processes in the absence of heat release by using helium as a fuel simulant.

Furthermore, these experiments are referred to as “cold flow” because the range of air total temperatures is significantly lower than the relevant flight total temperature. The low end of the range is bounded by the condensation limit for the expanding facility air and the high end by the thermal-structural limits of the uncooled hardware. The former and latter correspond to 728 and 978 K, respectively. Only the lower limit of the total temperature data are included in the current study. The use of “cold” flows and nonreacting fuel simulants for mixing experiments is not new[16] and has been extensively used as a screening technique for scramjet fuel injectors, and previously shown to be a good surrogate for the true flight environment by Drozda et al.[5]

The experimental data includes helium mole fraction and pitot pressures obtained with in-stream probes located downstream of the injection plane. A total of forty gas sampling probes, which double as pitot probes, are arranged vertically on a set of rakes. The vertical measurement spacing is 0.125 inches with the probe closest to the flat plate being a distance 0.40" from the plate. The rakes translate spanwise across the mixing flowfield at selectable survey planes perpendicular to the freestream flow direction. At each survey plane, measurements were obtained every 0.125" in the spanwise direction, over a 1" wide region centered about the center strut. A local gas sampling and analysis system provides the helium mole fraction of the gas captured by the gas sample probes at each probe position. The interested reader is referred to Cabell et al.[2] for a more detailed description of the gas sampling and analysis system. The end result of the mixing region flow surveys is helium mole fraction and pitot pressure distributions at multiple planes downstream of the injector. To date, surveys have been obtained at axial distances of 0.50, 1.0, 2.0, 4.0 and 6.0 inches downstream of the injection plane and are shown in Fig. 2. Additional surveys are planned at several farther downstream locations.

Previous analyses of Ground et al.[3] have shown that the substitution of pitot pressure for mass flux in the equation for mixing efficiency, Eq. 1, is a remarkably good approximation, at least for “cold flow", nonreacting

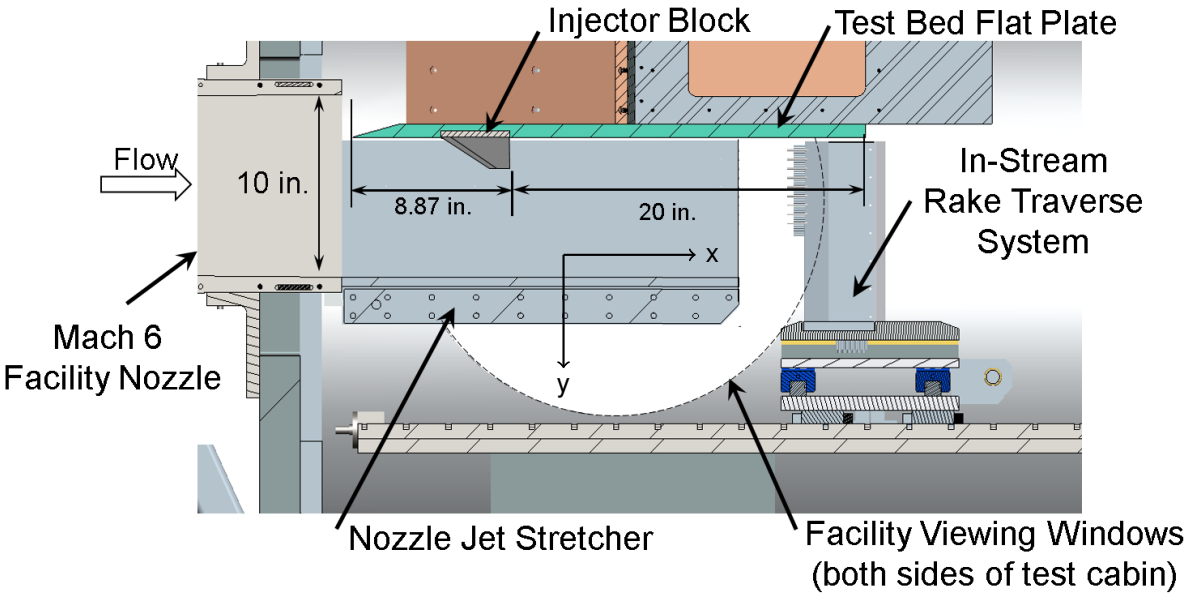

Figure 1. Cross section of the experimental cabin with the facility nozzle, test bed plate, jet-stretchers, instrumentation shroud, and the in-stream rake probe indicated. The figure shows the configuration as installed in the wind tunnel. All CFD simulations were performed with the positive y-direction in the plate-normal direction, which is pointing toward the ground.

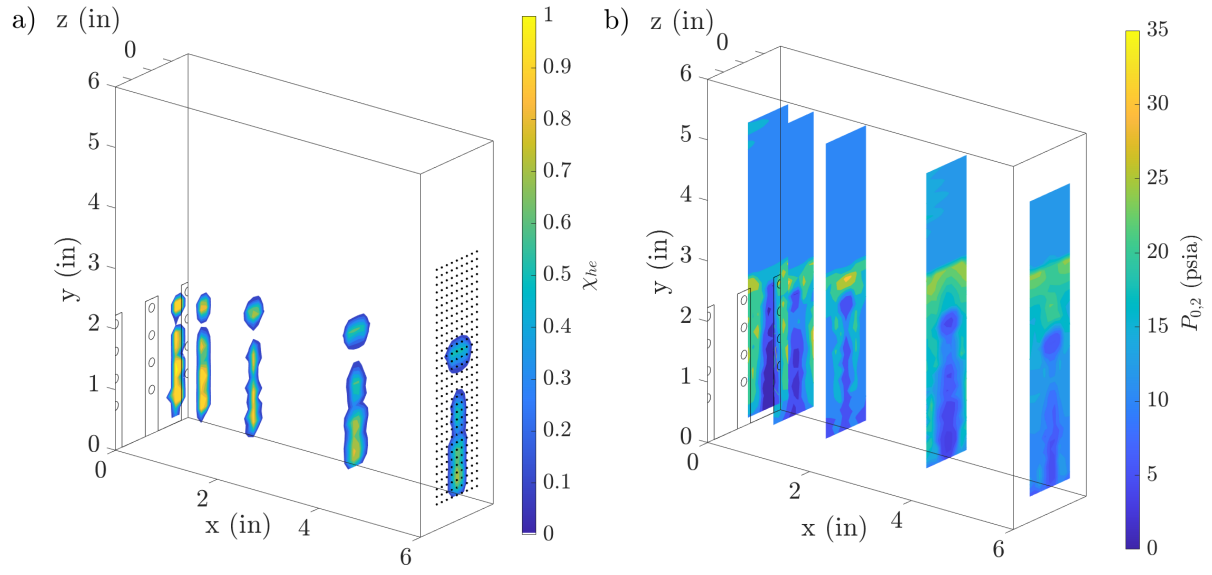

Figure 2. Contours of helium mole fraction (a), and pitot pressure (b) obtained experimentally at x = 0.5, 1, 2, 4, and 6 inches. At the x = 6 inches station the nominal experimental sampling grid is depicted.

mixing studies. This alternative pitot-based mixing efficiency, $\eta_m^{P_{0,2}}$ is thus:

$$\eta_m^{P_{0,2}} = \frac{\int \alpha_R P_{0,2} dA}{\int \alpha P_{0,2} dA}, \tag{4}$$

The advantage of $\eta_m^{P_{0,2}}$ is that the determination of the experimental mass flux distribution, which would otherwise require the measurement of three independent aerothermodynamic properties (e.g., static pressure, static temperature, and velocity) in addition to gas composition at each probe location, is not needed. Instead, the mixing efficiency can be accurately determined experimentally from only two relatively simple measurements of pitot pressure and gas composition. The experimental values of mixing efficiency shown in the results section are thus calculated from Eq. 4 by using the helium mole fraction (converted to mass fraction) and pitot pressure distributions shown in Fig. 2.

INJECTOR GEOMETRY AND FLOW CONDITIONS

An isometric view with dimensional details of the strut injector is shown in Fig. 3, where x, y, and z denote the streamwise (or downstream), vertical (or wall normal), and cross-stream directions, respectively. A row of nine strut injectors is placed 0.9 inches apart in the z-direction. This spacing is the same as that found in the previous work of Baurle et al.[17] Each strut injector has four fuel ports. The lower three ports are aligned with the x-axis, while the top-most port is rotated counterclockwise by 20 degrees in the xy-plane. Each injector port has a throat diameter of 0.083 inches followed by a conical expansion area with a half-angle of 6 degrees (not shown) that expands helium "fuel" to an exit Mach number of approximately 3.0.

The freestream conditions of the flow approaching the fuel injectors correspond to a total pressure and total temperature of 4.31 MPa and 728 K, respectively, expanded to a Mach number of about 6.4. A thermally perfect mixture of 21% oxygen (O_2), 78% nitrogen (N_2), and 1% nitric oxide (NO) by volume was used for the air. A small amount of NO was present to account for production of this species in the experimental

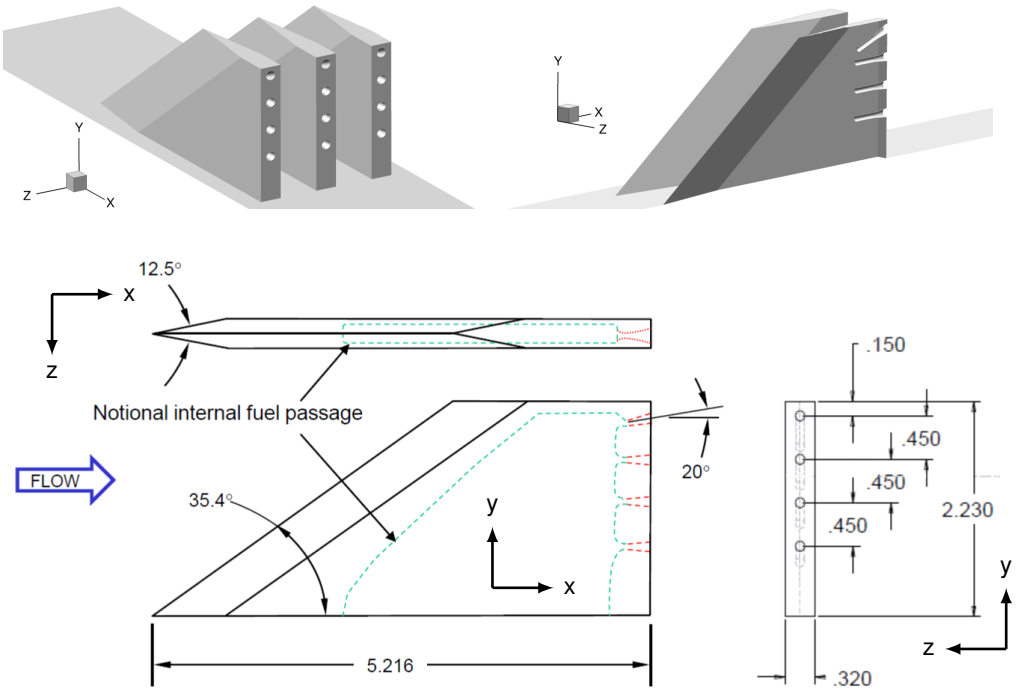

Figure 3. Isometric views and dimensional details of the baseline strut injector (dimensions are in inches).

facility,[18] although its impact on the current simulations is expected to be negligible. The mass flow rate of helium was set equal to the equivalent mass flow rate of hydrogen required to achieve an equivalence ratio (ER) of 0.75 over the intended fueling area (IFA) for this flow. The IFA is established based on a portion of the notional flow cross-section area that the injector is designed to fuel. The IFA for the strut was obtained from Baurle et al.[17] who investigated it in a ducted scramjet combustor configuration that was 3 inches high. Values of relevant global flow parameters for both fuel and air are provided in Table 1 for an ER of 0.75. All values are computed based on the flowpath entrance flow conditions for the air and the expanded flow conditions at the exit of the injector ports for the fuel. These values correspond to the nominal conditions used in the CFD simulations.

Table 1. Nominal facility air and fuel simulant (helium) flow conditions.

Property	Air†	Fuel Simulant (helium)
IFA ‡ W×H		0.9 × 3.0 (in^2)
Mach	6.41	2.98
$P0$ (MPa)	4.314	0.224
$T0$ (K)	728.1	293.15
P (kPa)	1.773	7.205
T (K)	80.67	74.14
u (m/s)	1155.8	1508.2

†21% O_2, 78% N_2, 1% NO by volume
‡Intended fueling area for the injector expressed as width times height (W×H)

NUMERICAL METHOD

The numerical simulations were performed using the Viscous Upwind aLgorithm for Complex flow ANalysis (VULCAN-CFD) code.[19] VULCAN-CFD is a structured/unstructured solver widely used for high-speed flow simulations. For this work, a structured, multiblock, cell-centered, finite-volume version of VULCAN-CFD was used for both RAS and LES. For RAS, the advective terms were computed using the Monotone Upstream-Centered Scheme for Conservation Laws (MUSCL) scheme[20] with the Low-Dissipation Flux-Split Scheme (LDFSS) of Edwards.[21] The governing equations were integrated using an implicit diagonalized approximate factorization (DAF) method.[22] The baseline blended $\mathrm{k}-\omega/\mathrm{k}-\epsilon$ turbulent physics model of Menter[14] was used for the majority of the simulations. RAS was also performed with a modified form of the k-equation, where the turbulent production term was modeled using the vorticity magnitude.[23] This strategy eliminated the production of artificially high turbulence levels behind strong shock waves, and tended to reduce the likelihood of turbulence variable realizability violations. A version of the Menter[14] model with quadratic constitutive relation (QCR)[24] was also used. This option invokes the constitutive relation for the Reynolds stresses instead of the linear Boussinesq relationship and is able to capture normal stress anisotropies, thereby providing improved RAS predictions for flows where this phenomenon is important. The current variant of the QCR model also includes the $2/3\rho\mathrm{k}$ contribution of the Boussinesq Reynolds stress tensor omitted in previous QCR formulations. A good resource for turbulence modeling for RAS is the NASA Langley Research Center Turbulence Modeling Resource website.[23] The Reynolds heat flux and species mass flux were modeled using a gradient diffusion model with turbulent Prandtl number $(\mathrm{Pr_t})$ and $\mathrm{Sc_t}$ of 0.9 and 0.5, respectively. To assess the sensitivity of the mixing flowfield to the latter, the value of $\mathrm{Sc_t}$ was set to 0.10, 0.25, 0.50, 0.75, and 1.00 for some of the simulations. Wilcox wall matching functions[25] were also used; however, their implementation in VULCAN-CFD includes a modification that allows the simulations to recover the integrate-to-the-wall behavior as the value of normalized wall-distance, $\mathrm{y^+}$, approaches one.[19] All simulations were converged until the total integrated mass flow rate and the total integrated heat flux on the walls remained constant to at least four decimal places. This typically occurred when the value of the $\mathrm{L_2}$-norm of the steady-state equation-set residual decreased by about 4–5 orders of magnitude. The thermodynamic properties of the mixture components were computed using the curve fits of McBride et al.[26] for both RAS and LES.

For LES, the hybrid RAS/LES methodology used in this effort is based on the framework originally developed by Baurle et al.,[12] with subsequent variants described by Choi et al.[27] and Boles et al.[28] This framework is designed to enforce a RAS behavior near solid surfaces, and switch to an LES behavior in the outer portion of the boundary layer and free shear layers. Hence, this formulation can be thought of as a wall-modeled LES approach, where a RAS closure is used as the near-wall model. The basic idea is to blend the RAS eddy viscosity value with the LES SGS viscosity, along with any transport equation that involves a common RAS and SGS property. In the current work, the blended k-ω RAS model of Menter[14] was blended with implicit LES (ILES), which relies on the numerical dissipation instead of an explicit SGS model for closure. Because of the absence of an explicit SGS model in LES, the subgrid Prandtl (Pr_{sgs}) and Schmidt (Sc_{sgs}) numbers are not required.

The hybrid RAS/LES used the low-dissipation numerical framework described by White et al.[29] and Baurle[30] to encourage and maintain the development of resolved turbulent content. In this effort, the $\kappa = 1/3$ MUSCL scheme was chosen as the dissipative reconstruction operator with the UNO limiter of Suresh and Huynh[31] to suppress spurious oscillations during this reconstruction process. A simple 4^{th}-order symmetric reconstruction scheme was chosen for the nondissipative operator. The final reconstructed states were obtained by blending the dissipative and nondissipative states by using a modified form of the Larsson sensor as described by Baurle.[32] The reconstructed density, pressure, and velocity variables were based solely on the sensor. However, a small fraction (20%) of the dissipative reconstruction was required for numerical stability when reconstructing the species mass fraction variables. The viscous fluxes were evaluated in the same manner as those for the RAS described above. The time-accurate hybrid RAS/LES solutions were advanced in time by using a dual time-stepping approach that combined a DAF scheme[22] for

integration in pseudotime, with a 3-point backward finite-difference approximation for integration in physical time.

The values selected for the flow evolution time step and subiteration CFL constraint were 5 ns and 5.0, respectively. The time step was chosen based on cell residence time considerations to ensure that turbulent structures would traverse less than one grid cell length per time step. The subiteration process was carried out until the residual error dropped approximately 2 orders of magnitude. This level of convergence typically required 3–5 subiterations for each time step.

The initial conditions for the hybrid RAS/LES flowfield were set to the converged RAS results for $\mathrm{Sc_t} = 0.5$. The simulations were monitored as a function of time to assess the establishment of a statistically stationary state prior to gathering flowfield statistics (or analyzing any instantaneous flow properties). Particular emphasis was given to the mass flow error and the integrated friction force time histories. Based on these metrics, a statistically stationary state was established after roughly 200,000 time-steps or about 1 ms. This integration period corresponded to four flow-through times, defined as the time required for the freestream particles to traverse the length of the simulation domain. After this time period, flowfield statistics were gathered for at least another 200,000 time-steps (additional four flow-through times).

To conserve the available computational resources, especially for LES, the computational domain was split into the upstream portion, which included the strut injector body, and a downstream portion, which included the mixing region downstream of the strut injector and the fuel injector ports. The upstream portion contained no fuel-air mixing and was simulated only once by using RAS with the intent to provide the inflow boundary condition for the downstream region for both RAS and LES. The turbulence model in the upstream region was limited to a small region adjacent to the flat plate. This approach allowed a turbulent boundary layer to form on the flat plate surface, but forced a laminar flow on the strut injector body side walls. The downstream portion of the domain included fuel-air mixing and was simulated using both RAS and LES with the flow conditions at the interface between the regions obtained from the upstream RAS. The downstream region extended to 10.25 inches downstream of the injection (interface) plane. For LES, the synthetic turbulence forcing at the LES inflow was not used, which was justified by the experimental observations near the inflow plane using PLIF.[33] Two grids, coarse and fine, each progressively finer by a factor of 2 in each of the three dimensions, were used for the downstream simulations. The grid resolutions are summarized for both regions in Table 2. The computational domain included a single strut injector with periodic boundary conditions used on the sides of the domain.

All grids were generated with GridPro[34] in the vicinity of the injector body and the leading edge of the flat plate, and further combined with Pointwise[35]-generated h-blocks to complete the computational definition of the geometry. The structured grid block topology and density along the centerline of the geometry are shown in Fig. 4. The strut injector body and the fuel injector ports are highlighted in blue and magenta, respectively. For the purpose of visualization, the fine mesh was coarsened by a factor of four in each dimension, and portions of the grids that extend to y=6 inches and the last section of the downstream grid that extends to x=10.25 inches were omitted. To support LES, the downstream grid is approximately uniform with the axial aspect ratio increasing to about 2 at 10 inches downstream.

The inflow of the upstream region and the outflow of the downstream region were placed 9 inches upstream and 10.25 inches downstream of the fuel injection plane (region interface), which is located at x = 0. Since the inflow boundary of the upstream region and the outflow boundary of the downstream region consist of supersonic flow, the mixture composition, static values of the temperature and pressure, and the Mach

Table 2. Number of computational nodes used for the upstream and downstream regions of the current simulations.

	Upstream	Downstream
Coarse	-	35,206,016
Fine	53,959,680	140,824,064

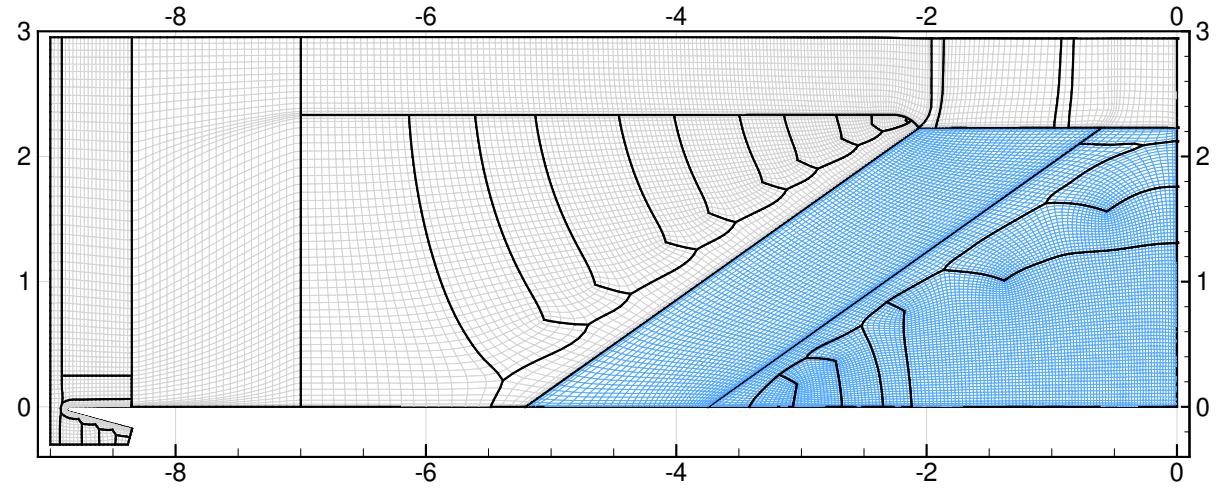

(a) Grid topology on and near the strut injector body for the upstream grid.

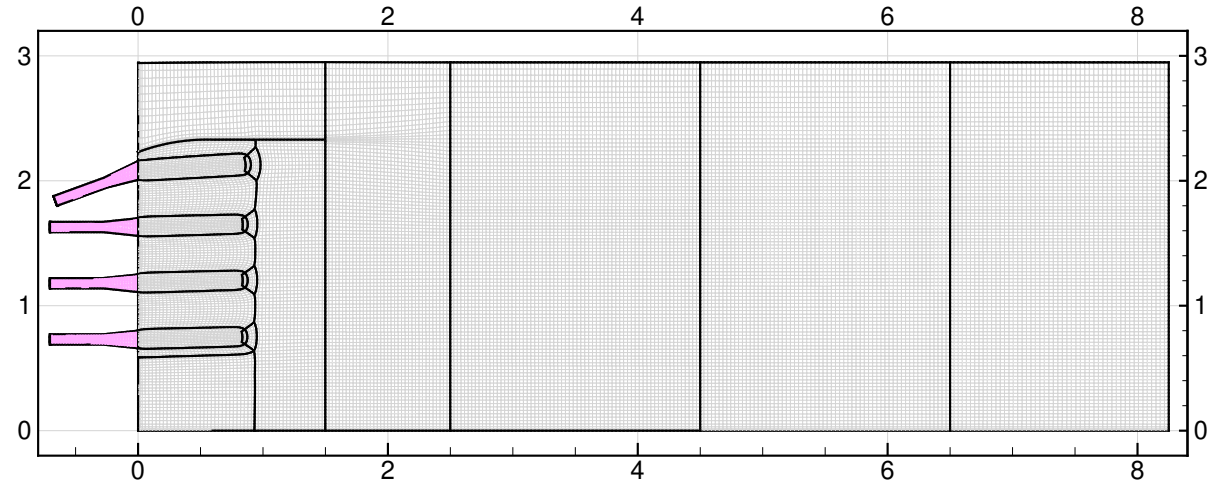

(b) Grid topology on and near the fuel ports for the downstream grid.

Figure 4. Visualization of the structured grid topology and density along the geometry centerline for the upstream (a) and downstream (b) regions of the simulation. The sections of the grids that extend to y=6 inches and the last section of the downstream grid that extends to x=10.25 inches were omitted. Each visible cell contains 4x4x4 cells on the actual fine mesh. The blue and magenta elements denote the injector body and the fuel ports, respectively.

number are specified at the inflow, and all flow variables are extrapolated at the outflow. Slip wall boundary conditions were used for the upper boundary of the flow domain. This upper boundary is 6 inches away from the flat plate, which approximates the height of the facility nozzle core flow. Because the simulation domain implies an infinite row of injectors in the cross-stream, the current simulations model the experiment as an infinitely wide duct. In this modeled 6-inch high duct, the flow blockage due to strut injector body is about 7%, unlike in the experiments that allow for complete blockage relief because of the open flat plate configuration. With the exception of the fuel ports, the grid was clustered toward all the walls with the growth rates varying from 5–15%. The values of y^{+} for these current flow conditions, obtained on a fine mesh, were

no greater than about 2 on the flat plate, with the largest values of approximately 20 observed on the strut injector leading edge, side walls, and fuel port walls. The values of y^+ are about two times larger for the coarse mesh.

Both RAS and LES were performed on a distributed memory cluster containing compute nodes with dual Intel Xeon Gold 6330 CPUs (56 compute cores/node) using the same fine grid. The RAS simulations required approximately 120k iterations to converge, which took 12 hours on 1980 compute cores (1hr/10k iterations). The LES simulations required approximately 400k iterations, which took 240 hours using 1944 compute cores (6hrs/10k). For LES simulations, a single flowthrough time took about 50k iterations, and four flowthrough times were run to flush out any residual initial condition. Additional four flowthrough times were run to compute the flow statistics. For the current simulations, LES is approximately an order of magnitude more computationally expensive than RAS.

RESULTS AND DISCUSSION

Because fuel-air mixing only takes place in the downstream simulation region, and the upstream region is only used to obtain the inflow conditions for the downstream region simulations, the results are focused on the downstream region only. To that end, contour plots of the time-averaged and instantaneous values of the Mach number obtained from RAS and LES, respectively, in the z-planes through the center of the injector ports, and x-planes at various locations are shown in Fig. 5. The RAS results are obtained with the Menter turbulence model[14] and $\mathrm{Sc_t} = 0.50$. The instantaneous LES result was obtained at 497.50μs after the start of the simulation, which corresponds to about two flowthrough times. These results demonstrate the development of the turbulent structures downstream of the injection plane. Because the inflow boundary condition does not incorporate synthetic turbulent fluctuations, unperturbed laminar flow features persist for about 1 inch downstream of the injection plane before the flow transitions to a turbulent state. The inclusion of synthetic turbulent fluctuations would potentially reduce this development length but could not eliminate it.[36] Nevertheless, previous experimental visualizations of the strut injector configuration with PLIF gave some indication that a laminar or transitional flow was expected on the strut sidewalls upstream of the injection plane,[33] thereby providing some justification for omitting synthetic fluctuations at the inflow plane. The boundary layer in the hybrid RAS/LES lacks any resolved turbulent content until about x=6 inches, where turbulent structures begin to develop. Because the interaction between the boundary layer and the mixing region above it is limited, this modeling limitation is not expected to significantly impact the results. Contour plots of the instantaneous values of the mass fraction of helium obtained after two flowthrough times from LES in the z-planes through the center of the injector ports, and x-planes at various locations are shown in in Fig. 6. These results further support the assertion that the turbulent structures begin rapid development at about 1 inch downstream of the injection plane and that the interaction between the mixing field and the boundary layer is limited.

Contour plots of the time-averaged values of the Mach number obtained from RAS and LES in the z-planes through the center of the injector ports, and x-planes at various locations are shown in Fig. 7. The x-plane locations are separated by 0.5 inches, starting with x=0.01 inches. The RAS results here are obtained with the Menter turbulence model[14] with QCR and $\mathrm{Sc_t} = 0.50$. The white isolines denote a helium mass fraction of 0.03, which represents stoichiometry of hydrogen. Overall, the qualitative flow features of RAS compare well with those in the LES.

The line plot of the one-dimensional values of the mixing efficiency versus distance for: RAS with several values of the $\mathrm{Sc_t}$ and computed with vorticity-based production and QCR options to the baseline Menter turbulence model, LES obtained on fine and coarse grids, and the preliminary experimental data, are shown in Fig. 8. The comparison between the mixing efficiency formulation based on mass flux (Eq. 1) and the pitot pressure (Eq. 4) for the Menter model with QCR is also shown. The difference between these formulations is relatively small, as previously demonstrated by Ground et al.,[3] justifying the use of a pitot pressure formulation to simplify the experiments. As expected, because the turbulent diffusion, and hence turbulent

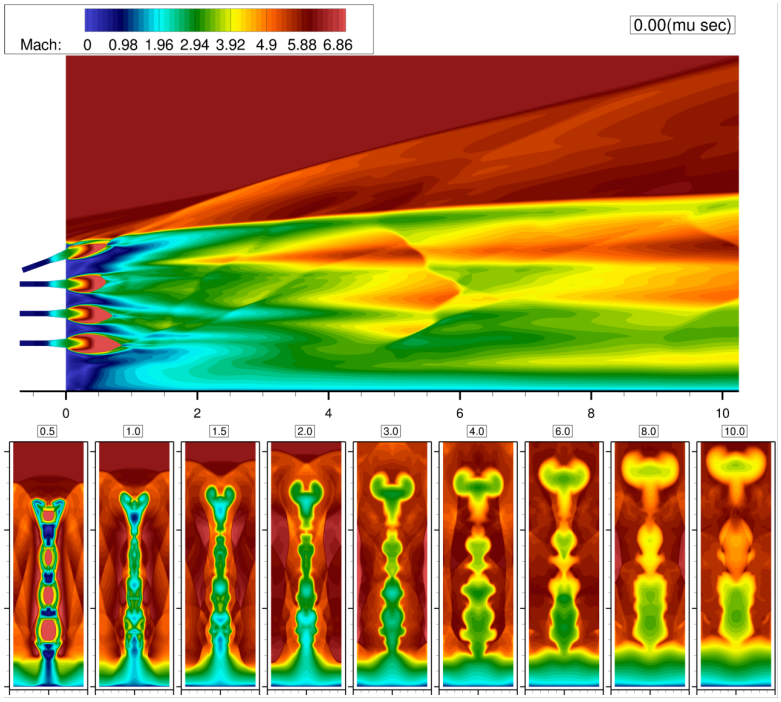

(a) Contour plot of Mach number obtained from RAS with the Menter turbulence model[14] and $\mathrm{Sc_t} = 0.50$.

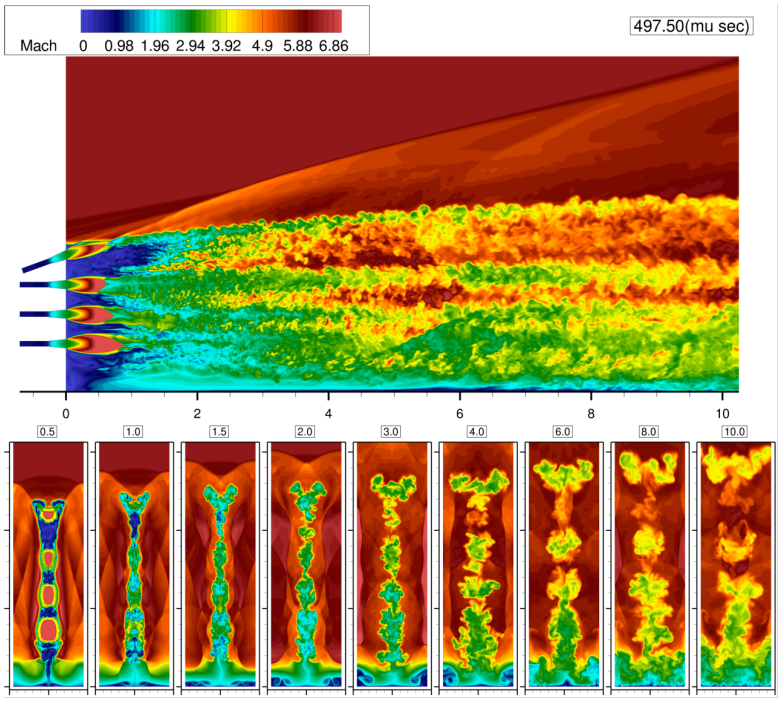

(b) Contour plot of the instantaneous Mach number obtained from LES.

Figure 5. Contour plots of the average and instantaneous Mach number obtained from RAS (a) and LES (b). Distance is in inches. The instantaneous image was obtained after two flowthrough times.

mixing, is inversely proportional to the $\mathrm{Sc_t}$, the mixing efficiency decreases for RAS with increasing values of the $\mathrm{Sc_t}$. Consequently, the mixing efficiency, and combustion efficiency for reacting flows, are very sensitive to this modeling parameter. This is one of the core reasons why, for propulsion applications, RAS requires experimental data to select a reasonable value of the $\mathrm{Sc_t}$. The impact of the vorticity-based production or QCR modifications to the baseline Menter model with $\mathrm{Sc_t} = 0.5$ on the mixing efficiency are also shown. Both appear to produce a relatively small increase in the mixing efficiency, such that the impact from simply decreasing the $\mathrm{Sc_t}$ from 0.50 to 0.25 is more significant.

The mixing efficiency obtained from the LES by using the fine and coarse meshes is also shown in Fig. 8. The error bars for the LES are estimated using the Grid Convergence Index (GCI),[37] which is based on Richardson extrapolation. The details of the implementation of the GCI used here are described in the VULCAN manual.[19] However, the GCI is used in a somewhat unconventional manner here because LES is not expected to achieve grid convergence, rather the LES result will approach a direct numerical simulation (DNS) result as the grid resolution is increased. Nevertheless, assuming that the approach toward the

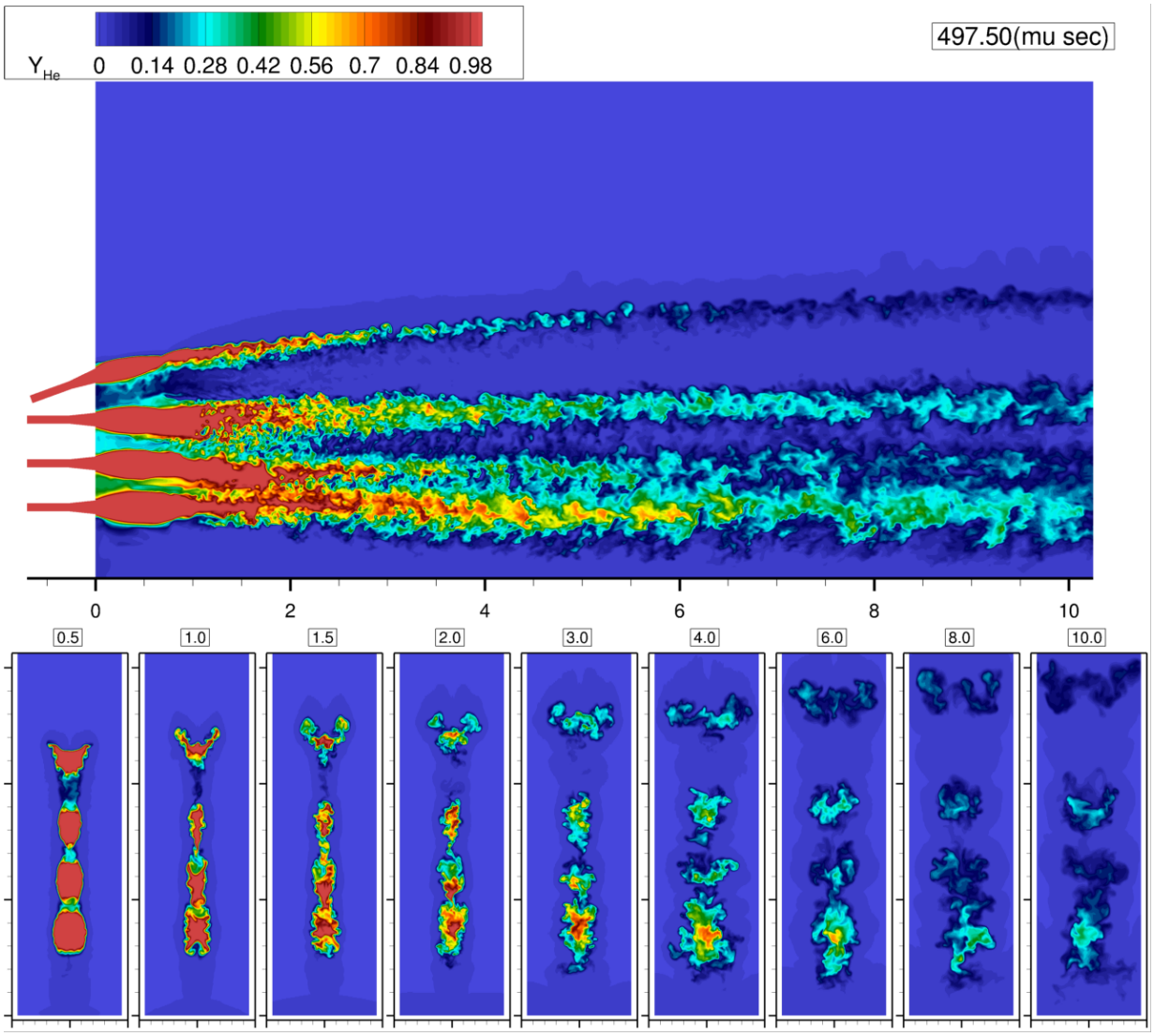

Figure 6. Contour plots of the instantaneous mass fraction of helium from LES. Distance is in inches. The instantaneous image was obtained after two flowthrough times.

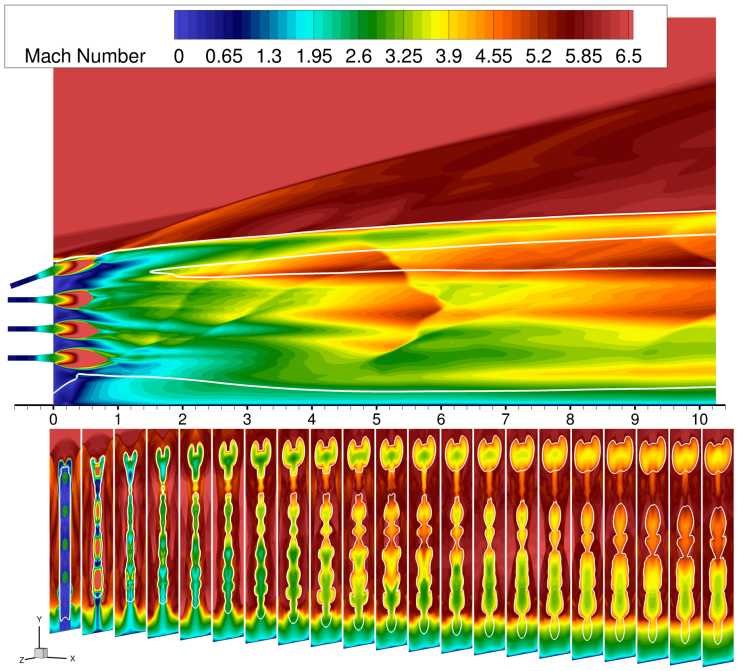

(a) Contour plot of Mach number obtained from RAS with the Menter turbulence model[14] with QCR and $\mathrm{Sc_t} = 0.50$.

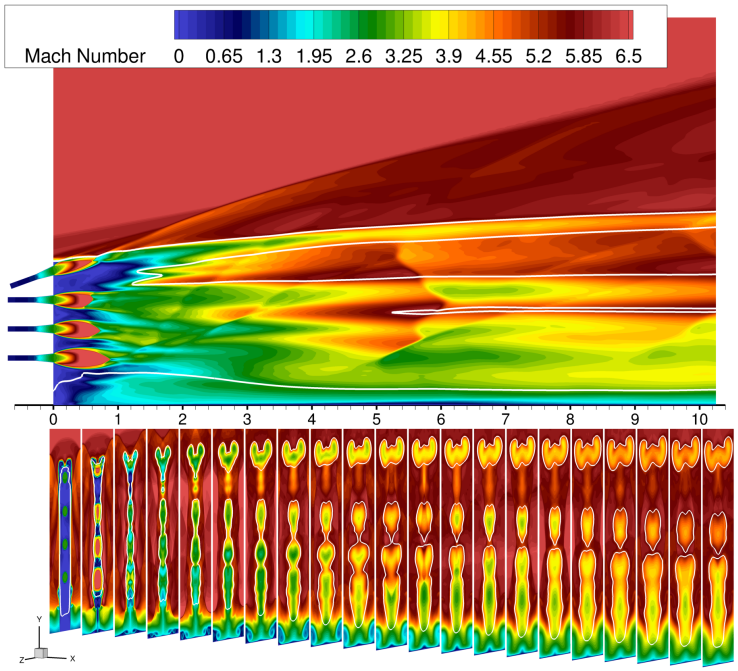

(b) Contour plot of the time-averaged Mach number obtained from LES.

Figure 7. Contour plots of the time-averaged Mach number obtained from RAS (a) and LES (b). Distance is in inches. The cross-planes are spaced 0.5 inches apart starting with x=0.01 inches. The white isolines denote a helium mass fraction of 0.03.

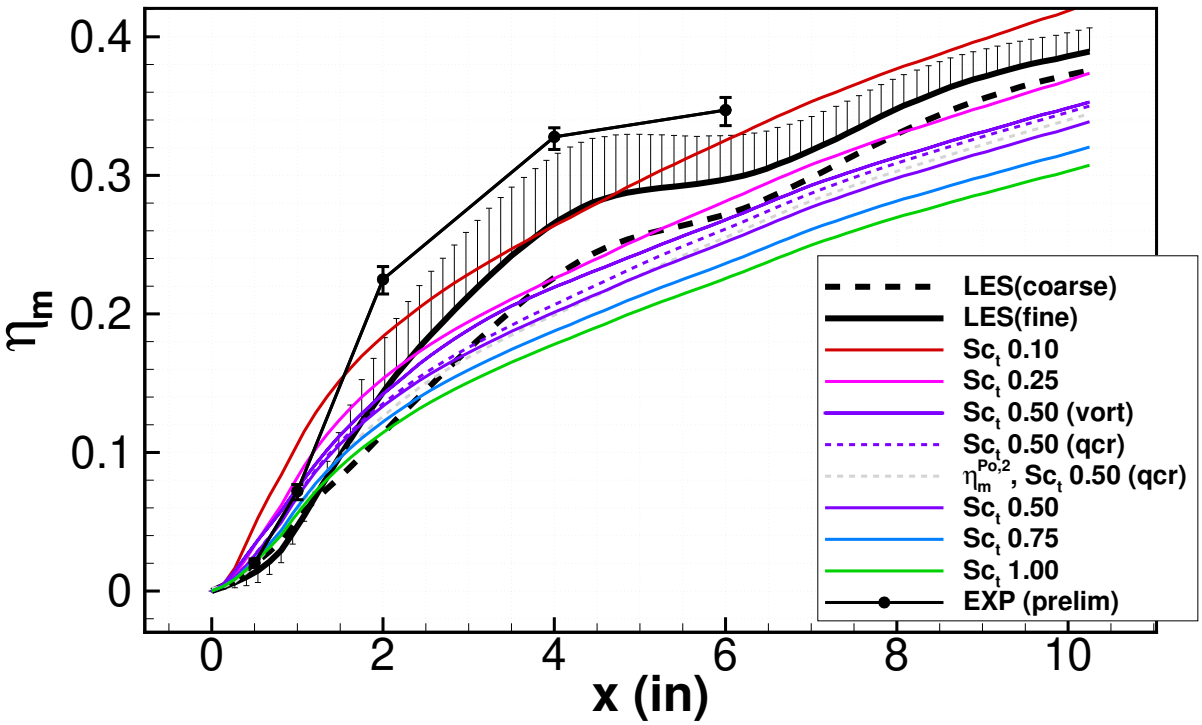

Figure 8. Line plot of the one-dimensional values of the mixing efficiency versus distance for RAS with several values of the $\mathrm{Sc_t}$ and vorticity-based production and QCR options to the baseline Menter turbulence model, LES obtained on fine and coarse grids, and the preliminary experimental data of EIMP.

DNS solution follows the same "pattern" as that from coarse to fine solution, and is not dominated by the truncated higher-order Taylor series terms used to derive the GCI expression, the error bars provide an estimate of a region where possible, further refined, LES solutions could reside. Unfortunately, verifying this application of the GCI is computationally expensive because further refining the LES mesh by a factor of two in each dimension would result in 8 times larger LES grid, which would also require halving the simulation time step, resulting in a 16 fold increase in time to solution, which would increase LES simulation time from about 240 hours to over 3800 hours (over 5 months). In the nearfield (x<1 inch), the mixing efficiency obtained from RAS demonstrates a rapid increase in values, whereas those obtained from LES are somewhat suppressed. This is the consequence of the flow transitioning from effectively laminar to turbulent. The mixing efficiency from LES on the coarse grid exhibits slightly higher values in the nearfield than those on the fine grid because the numerical diffusion, which effectively acts like turbulent mixing, is higher on the coarse grid. This effect is also found in RAS, where the mixing efficiency is typically found to be higher on coarse meshes.[4]

For LES, however, once the turbulence begins to rapidly develop beyond the nearfield, the fine grid supports a broader range of turbulent eddy structures, which rapidly mix fuel and air via the effect of resolved turbulent action. In RAS, the same effect is modeled by a "smooth" increase in the turbulent diffusion gradient, which is inversely proportional to the $\mathrm{Sc_t}$. As a consequence of increased turbulence resolution on the fine mesh, the LES actually predicts higher values of the mixing efficiency than those obtained on the coarse mesh. In the farfield (x>4 inches), the mixing efficiency curve obtained from the LES appears to settle between RAS results obtained with $\mathrm{Sc_t}$ of 0.1 and 0.25, respectively.

The preliminary experimental data indicate that in the nearfield the mixing develops more rapidly for experiments than for the LES but somewhat less rapidly than RAS, which is consistent with previous assertions that the flow upstream of the injection plane at x=0 is transitioning from laminar to fully turbulent flow. Downstream, the mixing efficiency rapidly increases and remains higher for all simulations. However, the region of suppressed mixing between x=4–6 inches captured by the LES appears to also be captured by the experimental data, although additional downstream measurements are needed to confirm this. At the moment, the most likely explanation why the LES, and to a lesser degree, the error bar estimates underpredict the experimental data has to do with the lack of quantitative information about the inflow. It is possible that some modest amount of synthetic turbulence fluctuations could accelerate the nearfield transition process and thereby enhance the nearfield mixing rate, which would "lift" the entire mixing efficiency curve. Despite this shortcoming, the general trend of the mixing efficiency curves match between RAS, LES and the experiment.

Although some experimental data, which includes flow visualization and gas sampling,[33] are available for this flow, in general, flowfield measurements for high-speed flows are challenging. At the same time, although computationally expensive, a few LES can often be performed. Therefore, it has been suggested that LES data can serve as a surrogate for the experimental data. One straightforward approach was demonstrated above, where a mixing efficiency was obtained from the LES and compared to that obtained from RAS with various models and/or parameters of interest (e.g., $\mathrm{Sc_t}$). For the current simulations, Fig. 8 suggests that a value of $\mathrm{Sc_t}$ in the range of 0.1–0.25, perhaps 0.2, would be appropriate to approximate the LES result with the Menter turbulence model. The low value of $\mathrm{Sc_t}$ is somewhat surprising because practical experience with RAS suggests values in the range of 0.5–0.75 are more common. The downside of the direct comparison approach is the requirement to run several RAS for a range of modeling parameters of interest, which is cumbersome, and which may produce several combinations of options that match the LES, leaving the analyst guessing at the right combination. For example, if various turbulence models and/or their options produce different mixing efficiency curves, which they do as demonstrated for the current case by Drozda et al.,[10] then simultaneously varying the $\mathrm{Sc_t}$ will also produce different values that match the target LES data leaving the user wondering which turbulence model and $\mathrm{Sc_t}$ combination is appropriate.

To help address this, another approach is to process the resolved LES data in such a way as to extract RAS turbulence modeling parameters. For example, to determine the "best fit" $\mathrm{Sc_t}$ value from the LES data, a scatter plot of the correlation between the functional form of the RAS diffusion model and the LES data was generated. Standard RAS models, including the Menter model used in this work, assume that the Reynolds stress tensor is correlated with the mean strain rate, while the Reynolds mass flux vector is correlated to the mean mass fraction gradient, i.e.,

$$\tau_{ij} \;=\; 2\mu_t\left(S_{ij}-\frac{1}{3}\delta_{ij}\frac{\partial\tilde{u}_k}{\partial x_k}\right) \;-\; \frac{2}{3}\delta_{ij}\bar{\rho}\tilde{k}\;, \qquad\qquad \widetilde{\bar{\rho}u_i^{"}Y_m^{"}} \;=\; -\frac{\mu_t}{\mathrm{Sc_t}}\frac{\partial\tilde{Y}_m}{\partial x_i}. \tag{5}$$

A least-squares minimization procedure can be used to determine the "best fit" μ_t value that correlates the Reynolds stress tensor to the mean strain rate. The same procedure can be applied to determine the "best fit" μ_t / $\mathrm{Sc_t}$ value that correlates the Reynolds mass flux vector to the mean mass fraction gradient to arrive at the following relationships:

$$\mu_t \;=\; \frac{\left(\tau_{ij}+\frac{2}{3}\delta_{ij}\bar{\rho}\tilde{k}\right)\left(S_{ij}-\frac{1}{3}\delta_{ij}\,\frac{\partial\tilde{u}_k}{\partial x_k}\right)}{2\left(S_{ij}-\frac{1}{3}\delta_{ij}\frac{\partial\tilde{u}_k}{\partial x_k}\right)\left(S_{ij}-\frac{1}{3}\delta_{ij}\frac{\partial\tilde{u}_k}{\partial x_k}\right)} \;\equiv\; \frac{\tau_{ij}^*\;S_{ij}^*}{2\;S_{ij}^*\;S_{ij}^*}\;, \qquad\qquad \frac{\mu_t}{\mathrm{Sc_t}} \;=\; \frac{-\widetilde{\bar{\rho}u_i^{"}Y_m^{"}}\frac{\partial\tilde{Y}_m}{\partial x_i}}{\frac{\partial\tilde{Y}_m}{\partial x_i}\frac{\partial\tilde{Y}_m}{\partial x_i}}. \tag{6}$$

The least-squares "best fit" $\mathrm{Sc_t}$ value is then obtained on a cell-by-cell basis by using the above relationships. Combining Eqs. 6, we can obtain a functional form where the $\mathrm{Sc_t}$ appears as a "slope" of a line, which can be extracted from the plot of the LES data:

$$\underbrace{\tau_{ij}^*\;S_{ij}^*\;\frac{\partial\tilde{Y}_m}{\partial x_i}\frac{\partial\tilde{Y}_m}{\partial x_i}}_{\mathrm{y(Sc_t)}} = \underbrace{-\mathrm{Sc_t}\left(\widetilde{\bar{\rho}u_i^{"}Y_m^{"}}\frac{\partial\tilde{Y}_m}{\partial x_i}\;2\;S_{ij}^*\;S_{ij}^*\right)}_{\mathrm{x(Sc_t)}}. \tag{7}$$

Figure 9 shows a scatter plot of the $\mathrm{y}(\mathrm{Sc_t})$ versus $\mathrm{x}(\mathrm{Sc_t})$ terms of Eq. 7. The scatter data are limited to helium mass fractions of 0.001–0.999 to exclude pure fuel or air regions where $\mathrm{Sc_t}$ would be undefined. Nearfield data for x<1 inch are also excluded because the flow in this region is laminar or transitional, as discussed above, hence a turbulent mixing modeling parameter holds limited relevance for this region. The contours of the Mach number for the scatter plot data are plotted at various x-plane locations, starting with x=1.51 and separated by 0.5 inches are shown in Fig. 9. To verify the approach, Fig. 9(a) shows the scatter plot of the RAS data obtained with the Menter[14] turbulence model and $\mathrm{Sc_t} = 0.50$. As expected, the least-squares "best fit" approach shows a scatter of RAS data closely following the $\mathrm{Sc_t} = 0.5$ line. The data do not collapse exactly onto this line primarily because of interpolation used to project the RAS data from cell centers to nodes for postprocessing, and because all gradients in Eq. 6 are computed in postprocessing, which introduces an inconsistency with those computed in the solver to obtain μ_t. Nevertheless, a clear indication of the expected correlation for the RAS data exists.

For the scatter obtained from the LES data shown in Fig. 9(b), no single obvious $\mathrm{Sc_t}$ value that collapses all data can be discerned. This is expected because the closure models used for RAS are far from perfect (e.g., nongradient effects may influence the Reynolds mass flux vector). However, there is a clustering of points that corresponds to a slope ($\mathrm{Sc_t}$ value) of about 0.6–0.7, as denoted by the green lines on the plot, suggesting this to be the proper range of values given the constraint of a constant $\mathrm{Sc_t}$ value imposed by the standard gradient diffusion assumption. A similar $\mathrm{Sc_t}$ value was deduced by Zilberter and Edwards[38] when the same procedure was applied to a series of high-speed mixing layers and a supersonic jet-in-crossflow problem.

However, the direct comparison of the mixing efficiency obtained from RAS and LES indicated that a value of $\mathrm{Sc_t}$ in the range of 0.1–0.25 would be appropriate to approximate the LES result with the Menter turbulence model, whereas the least-squares "best fit" approach indicates that a value in the range of 0.6–0.7 should be used. Since the least-squares "best fit" approach has been verified with RAS, the implication is that the Menter turbulence model is not accurately modeling the physics of this flowfield, and that adjusting the $\mathrm{Sc_t}$ to 0.1–0.25 corrects for the model deficiencies, albeit perhaps for the wrong reasons. Figure 10 shows a turbulence model and $\mathrm{Sc_t}$ sensitivity analysis performed for the strut injector at similar flow conditions by Drozda et al.[10] All the turbulence models used in this comparison are representative of those used in practical applications. These were: Menter-BSL and -SST,[14] Wilcox-1998 and -2006,[39] and the explicit algebraic Reynolds-stress model (EARSM) of Rumsey and Gatski.[40] Among those, the Menter-BSL model is used in the current work. The models and their common implementations are described in detail on the NASA Langley Research Center Turbulence Modeling Resource website.[23] Simulations were also performed with the Wilcox-1998 and -2006 models without the round-jet/planar-jet anomaly corrections[25] typically included with these models and denoted by -NP on Fig. 10. The results of this prior study demonstrated the large sensitivity of the the mixing efficiency to the choice of the turbulence model and $\mathrm{Sc_t}$ used in RAS. These results also suggest that the Wilcox-2006-NP model, or perhaps the EARSM, could be good candidates for the current flow because they predict increased mixing with $\mathrm{Sc_t} = 0.5$ as compared to the Menter-BSL model. These observations are also consistent with those of Baurle[30] who found that the EARSM model with the $\mathrm{Sc_t} = 0.7$ performed well for RAS of the model scramjet cavity flow experiment.

Motivated by these observations, four additional RAS simulations were performed. These used Wilcox-2006-NP and the EARSM turbulence models with vorticity-based production, and $\mathrm{Sc_t} = 0.6$ and 0.7, which bound the range found from the LES scatter data in Fig. 9. Figure 11 shows line plots of the one-dimensional values of the mixing efficiency versus distance for those models. LES and the preliminary experimental data are also shown. The mixing efficiency values for these two turbulence models match those of the LES data in the nearfield (x<2 inches). However, neither of the RAS models is able to capture the mixing enhancement-suppression region (2<x<7 inches) that LES and the experiment reveal. In the farfield (x>7 inches), the Wilcox-2006-NP model with $\mathrm{Sc_t} = 0.7$ matches both value and the slope of the LES data, while the EARSM model overpredicts the mixing efficiency.

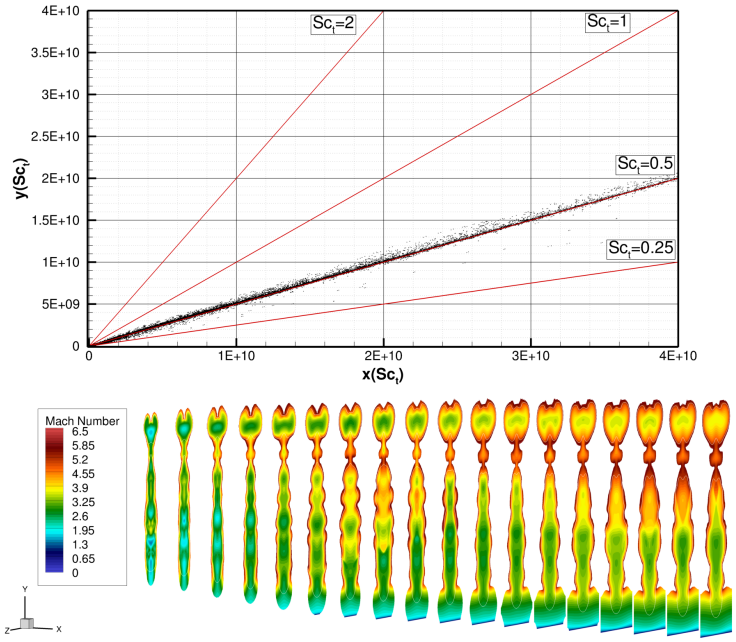

(a) RAS with $\mathrm{Sc_t} = 0.5$.

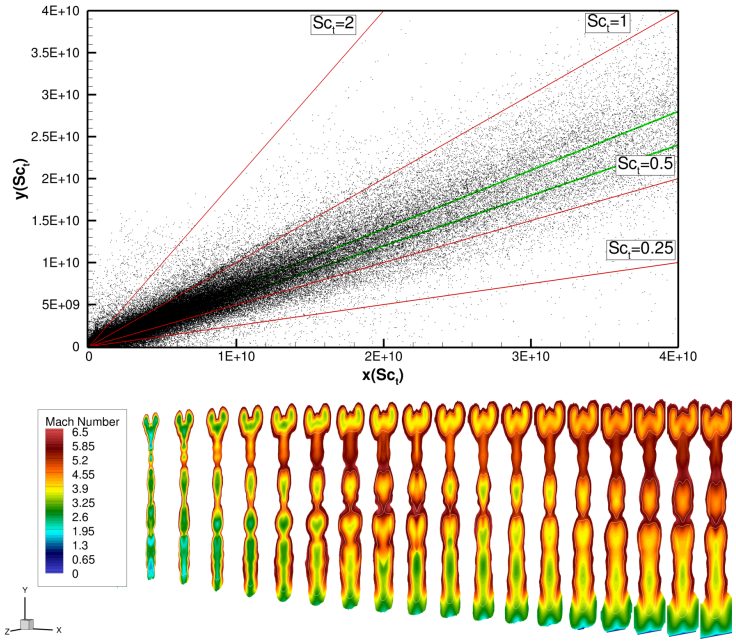

(b) LES. Green lines denote $\mathrm{Sc_t}$ range of 0.6–0.7

Figure 9. Scatter plot of the $\mathrm{y(Sc_t)}$ versus $\mathrm{x(Sc_t)}$ of Eq. 7, and contours of the Mach number for the scatter plot data are plotted at various x-plane locations starting, with x=1.51 and separated by 0.5 inches. Green lines denote $\mathrm{Sc_t}$ range of 0.6–0.7.

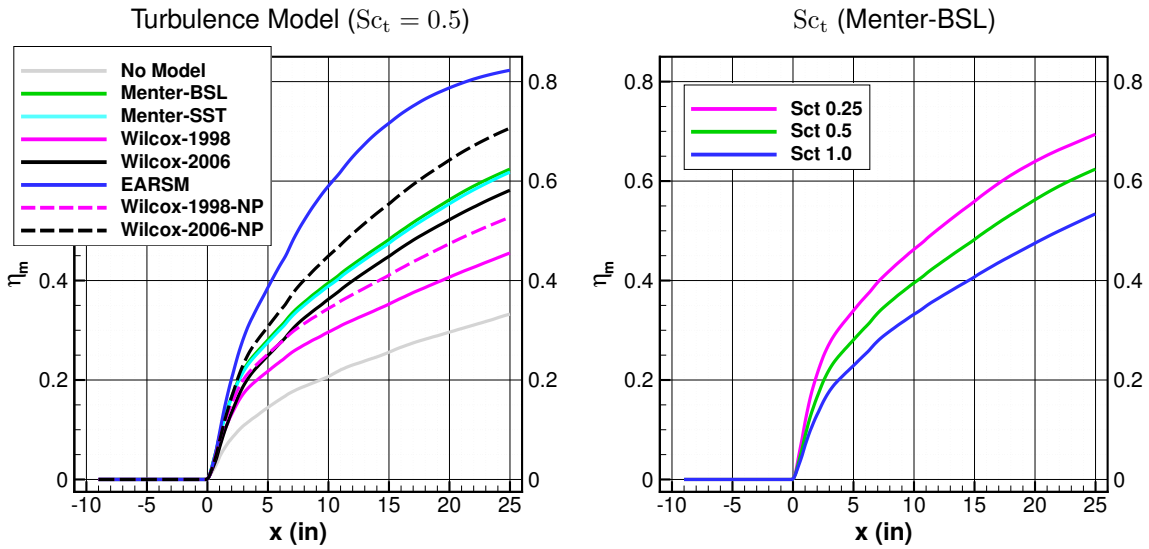

Figure 10. Line plot of the one-dimensional values of the mixing efficiency versus distance for RAS with several different turbulence models with $\mathrm{Sc_t} = 0.5$, and for RAS with several different values of $\mathrm{Sc_t}$ with Menter-BSL turbulence model. Reproduced from Drozda et al.[10]

SUMMARY AND CONCLUSIONS

Mixing efficiency is obtained for a strut fuel injector at hypervelocity flow conditions using RAS, LES, and experiments. The injector and flow conditions have been previously investigated using RAS and experiments as a part of the Enhanced Injection and Mixing Project (EIMP) at the NASA Langley Research Center (LaRC). The RAS uses the two-equation linear eddy viscosity and diffusivity modeling of Menter. In RAS, the species diffusivity model exhibits a strong dependence on the $\mathrm{Sc_t}$, which is often adjusted until some metric of engineering interest, such as the mixing efficiency, matches the experimental data. In absence of experimental data, LES has been proposed as a surrogate for experiments, that could provide the data needed to "calibrate" the $\mathrm{Sc_t}$ in the RAS models. The current simulations were intended to assess the feasibility of LES to serve as a surrogate for the experimental data, where the latter are not available or readily obtained. For the current case, limited preliminary gas sampling data are available; however, the mixing efficiency values obtained from RAS and LES significantly underpredict those calculated from the experiments. Nevertheless, the mixing efficiency curves obtained from the LES on the coarse and fine grids were directly compared to those of RAS where the $\mathrm{Sc_t}$ varied from 0.1–1.0. The comparisons revealed that RAS with $\mathrm{Sc_t}$ in the range of 0.1–0.25 could match the LES results.

LES results were also postprocessed using a least-squares "best-fit" approach to extract an approximate value of the $\mathrm{Sc_t}$ that should be used with a RAS gradient diffusion model. This approach found that a $\mathrm{Sc_t}$ value of about 0.6–0.7 should be used, which is consistent with practical experience, but does not match what was found by directly comparing the mixing efficiency curves. The discrepancy was attributed to the RAS model-form uncertainty, and suggested that for the Menter model, excessively small $\mathrm{Sc_t}$ values must be used to correct for model-form errors.

Revisiting prior work of Drozda et al.,[10] which investigated turbulence model sensitivity for the strut injector, albeit at slightly different flow conditions, identified two model candidates, namely the Wilcox-2006 model without the round-jet/planar-jet anomaly correction, and the explicit algebraic Reynolds-stress model of Rumsey and Gatski[40] as potentially more consistent with the LES predictions of the mixing efficiency and the least-squares "best-fit" approach estimates for $\mathrm{Sc_t}$. Additional RAS with the Wilcox-2006 and EARSM

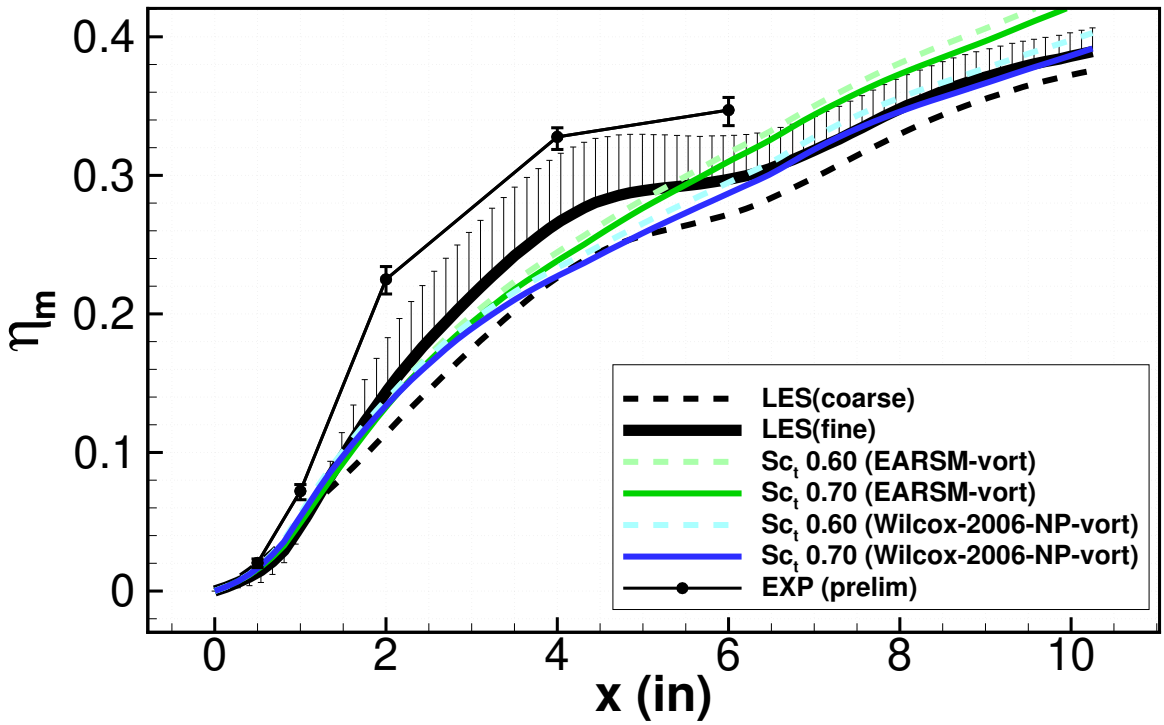

Figure 11. Line plot of the one-dimensional values of the mixing efficiency versus distance for RAS with Wilcox-2006-NP and EARSM turbulence models and two values of the $\mathrm{Sc_t}$ bounding the range found from LES. LES on fine and coarse grids, and the preliminary experimental data of EIMP are also shown.

models demonstrated that the Wilcox-2006 model with $\mathrm{Sc_t} = 0.7$ was able to reproduce the LES data in both nearfield and farfield of the mixing region. The mixing-suppressed region resolved by the LES could not be captured by any RAS.

In summary, it may not always be feasible to use the LES as a surrogate for the experimental data due to uncertainties associated with the flow boundary conditions; however, the information LES provides can be leveraged to reduce the model-form and model-parameter uncertainty of RAS. The current work provided a real-world example of how an LES can be used in this manner. The specific reasons why the turbulent viscosity of various RAS models reproduced the LES data more or less accurately will be investigated in the future.

ACKNOWLEDGMENTS

This work is supported by the Hypersonic Technology Project (HTP) in the Advanced Air Vehicles Program (AAVP) of the NASA Aeronautics Research Mission Directorate (ARMD). Computational resources are provided by the NASA Langley Research Center and the NASA Advanced Supercomputing (NAS) Division.

REFERENCES

[1] Lee, J., Lin, K.-C., and Eklund, D., ***Challenges in Fuel Injection for High-Speed Propulsion Systems***, AIAA J., 53(6):1405–1423 (Jun. 2015).

[2] Cabell, K., Drozda, T. G., Axdahl, E. L., and Danehy, P. M., ***The Enhanced Injection and Mixing Project at NASA Langley***, in *JANNAF 46th CS / 34th APS / 34th EPSS / 28th PSHS Joint Subcommittee Meeting*, NTRS Report Number NF1676L-25526, Albuquerque, NM (Dec. 2014).

[3] Ground, C. R., Cabell, K. F., and Drozda, T. G., ***Analytical and Experimental Demonstration of an Alternate Mixing Performance Metric for High-Speed Fuel Mixing Studies***, in *AIAA Aviation Forum*, Virtual (Jun. 2020).

[4] Drozda, T. G., Drummond, J. P., and Baurle, R. A., ***CFD Analysis of Mixing Characteristics of Several Fuel Injectors at Hypervelocity Flow Conditions***, in *52nd AIAA/SAE/ASEE Joint Propulsion Conference*, AIAA, Salt Lake City, UT (Jul. 2016).

[5] Drozda, T. G., Baurle, R., and Drummond, J. P., ***Impact of Flight Enthalpy, Fuel Simulant, and Chemical Reactions on the Mixing Characteristics of Several Injectors at Hypervelocity Flow Conditions***, in *63rd JANNAF Propulsion Meeting / 47th CS / 35th APS / 345h EPSS / 29th PSHS Joint Subcommittee Meeting*, NTRS Report Number NF1676L-23113, Newport News, VA (May 2016).

[6] Drozda, T. G., Shenoy, R. R., Passe, B. J., Baurle, R., and Drummond, J. P., ***Comparison of Mixing Characteristics for Several Fuel Injectors on an Open Plate and in a Ducted Flowpath Configuration at Hypervelocity Flow Conditions***, in *JANNAF Meeting / 48th CS / 36th APS / 36th EPSS / 30th PSHS Joint Subcommittee Meeting*, NTRS Report Number NF1676L-27197, Newport News, VA (Dec. 2017).

[7] Drozda, T. G., Cabell, K. F., Ziltz, A. R., Hass, N. E., Inman, J. A., Burns, R. A., Bathel, B. F., Danehy, P. M., Abul-Huda, Y. M., and Gamba, M., ***Comparisons Between NO PLIF Imaging and CFD Simulations of Mixing Flowfields for High-Speed Fuel Injectors***, in *53rd AIAA/SAE/ASEE Joint Propulsion Conference, AIAA Propulsion and Energy Forum*, AIAA, Atlanta, GA (Jul. 2017).

[8] Drozda, T. G., Cabell, K. F., Ziltz, A. R., Hass, N. E., Inman, J. A., Burns, R. A., Bathel, B. F., and Danehy, P. M., ***Comparison Between NO PLIF Imaging and CFD Simulations of Mixing Flowfields for High-Speed Fuel Injectors***, in *JANNAF Meeting / 48th CS / 36th APS / 36th EPSS / 30th PSHS Joint Subcommittee Meeting*, NTRS Report Number NF1676L-27198, Newport News, VA (Dec. 2017).

[9] Shenoy, R. R., Drozda, T. G., Norris, A. T., Baurle, R. A., and Drummond, J. P., ***Comparison of Mixing Characteristics for Several Fuel Injectors at Mach 8, 12, and 15 Hypervelocity Flow Conditions***, in *AIAA Propulsion and Energy Forum*, Cincinnati, OH (Jul. 2018).

[10] Drozda, T. G., Lampenfield, J. J., Deshmukh, R. G., Baurle, R. A., and Drummond, J. P., ***The Effect of Turbulence Modeling on the Mixing Characteristics of Several Fuel Injectors at Hypervelocity Flow Conditions***, in *AIAA Scitech*, San Diego, CA (Jan. 2019).

[11] Slotnick, J., Khodadoust, A., Alonso, J., Darmofal, D., Gropp, W., Lurie, E., and Mavriplis, D., ***CFD Vision 2030 Study: A Path to Revolutionary Computational Aerosciences***, NASA Contractor Report 218178 (Jan. 2014).

[12] Baurle, R. A., Tam, C.-J., Edwards, J. R., and Hassan, H. A., ***Hybrid Simulation Approach for Cavity Flows: Blending, Algorithm, and Boundary Treatment Issues***, AIAA J., 41(8):1463–1480 (2003).

[13] Girimaji, S. S., ***Partially-Averaged Navier-Stokes Model for Turbulence: A Reynolds-Averaged Navier-Stokes to Direct Numerical Simulation Bridging Method***, J. Appl. Mech., 73(3):413–421 (2006).

[14] Menter, F. R., ***Two-Equation Eddy-Viscosity Turbulence Models for Engineering Applications***, AIAA J., 32(8):1598–1605 (Aug. 1994).

[15] Mao, M., Riggins, D. W., and McClinton, C. R., ***Numerical Simulation of Transverse Fuel Injection***, in *Computational Fluid Dynamics Symposium on Aeropropulsion*, NASA-CP-3078, pages 635–667, NASA, Cleveland, OH (Apr. 1990).

[16] McClinton, C. R., ***Evaluation of Scramjet Combustor Performance Using Cold Nonreactive Mixing Tests***, in *14th AIAA Aerospace Sciences Meeting*, Washington, DC (Jan. 1976).

[17] Baurle, R. A., Fuller, R. P., White, J. A., Chen, T. H., Gruber, M. R., and Nejad, A. S., ***An Investigation of Advanced Fuel Injection Schemes for Scramjet Combustion***, in *36th Aerospace Sciences Meeting and Exhibit*, Reno, NV (Jan. 1998).

[18] Cabell, K. F. and Rock, K. E., ***A Finite Rate Chemical Analysis of Nitric Oxide Flow Contamination Effects on Scramjet Performance***, Tech. Rep. TP-2003-212159, NASA (2003).

[19] VULCAN-CFD, ***http://vulcan-cfd.larc.nasa.gov/*** (2023).

[20] van Leer, B., ***Towards the Ultimate Conservative Difference Scheme. V: A Second-Order Sequel to Godunov's Method***, J. Comput. Phys., 32(1):101–136 (Jul. 1979).

[21] Edwards, J. R., ***A Low-Diffusion Flux-Splitting Scheme for Navier-Stokes Calculations***, Comput. Fluids., 26(6):635–659 (Jul. 1997).

[22] Pulliam, T. H. and Chaussee, D. S., ***A Diagonal Form of an Implicit Approximate-Factorization Algorithm***, J. Comput. Phys., 39(2):347–363 (Feb. 1981).

[23] Rumsey, C., ***NASA Langley Research Center Turbulence Modeling Resource***, https://turbmodels.larc.nasa.gov (2023).

[24] Mani, M., Babcock, D., Winkler, C., and Spalart, P., ***Predictions of a Supersonic Turbulent Flow in a Square Duct***, in *51st AIAA Aerospace Sciences Meeting and Exhibit*, AIAA, Grapevine, TX (Jan. 2013).

[25] Wilcox, D. C., ***Turbulence Modeling for CFD***, DCW Industries, Inc., La Cañada, CA (2006).

[26] McBride, B. J., Gordon, S., and Reno, M. A., ***Thermodynamic Data for Fifty Reference Elements***, NASA Technical Paper 3287/REV1, NASA, Cleveland, OH (Feb. 2001).

[27] Choi, J.-I., Edwards, J., and Baurle, R., ***Compressible Boundary-Layer Predictions at High Reynolds Number Using Hybrid LES/RANS Methods***, AIAA J., 47(9):2179–2193 (Sep. 2009).

[28] Boles, J. A., Choi, J.-I., and Edwards, J. R., ***Simulations of High-Speed Internal Flows Using LES/RANS Models***, in *47th AIAA Aerospace Sciences Meeting Including The New Horizons Forum and Aerospace Exposition*, AIAA, Orlando, FL (Jan. 2009).

[29] White, J. A., Baurle, R. A., Fisher, T. C., Quinlan, J. R., and Black, W. S., ***Low-Dissipation Advection Schemes Designed for Large Eddy Simulations of Hypersonic Propulsion Systems***, in *48th AIAA/ASME/SAE/ASEE Joint Propulsion Conference and Exhibit*, AIAA, Atlanta, GA (Jul. 2012).

[30] Baurle, R. A., ***Hybrid Reynolds-Averaged/Large-Eddy Simulation of a Cavity Flameholder: Modeling Sensitivities***, AIAA J., 55(2):524–543 (2017).

[31] Suresh, A. and Huynh, H. T., ***Numerical Experiments on a New Class of Nonoscillatory Schemes***, in *30th Aerospace Sciences Meeting and Exhibit*, Reno, NV (Jan. 1992).

[32] Baurle, R. A., ***Hybrid Reynolds-Averaged / Large Eddy Simulation of a Flow in a Model Scramjet Cavity Flameholder***, in *54th AIAA Aerospace Sciences Meeting*, San Diego, CA (Jan. 2016).

[33] Drozda, T. G., Ground, C. R., Knapp, W. T., and Danehy, P. M., ***Simple, Fast Nitric Oxide Planar Laser-Induced Fluorescence Model for Computational Fluid Dynamics Applications***, AIAA J., 61(4):1759–1771 (Feb. 2023).

[34] Program Development Company, ***GridPro - Automatic Multiblock Grid Generation Software***, http://www.gridpro.com/ (2017).

[35] Pointwise, Inc., ***Pointwise: Mesh Generation Software for CFD***, http://www.pointwise.com/ (2017).

[36] Jarrin, N., Prosser, R., Uribe, J.-C., Benhamadouche, S., and Laurence, D., ***Reconstruction of Turbulent Fluctuations for Hybrid RANS/LES Simulations Using a Synthetic-Eddy Method***, Int. J. Heat. Fluid. Fl., 30(3):435–442 (Jun. 2009).

[37] Roache, P. J., ***Verification and Validation in Computational Science and Engineering***, Hermosa Publishers (1998).

[38] Zilberter, I. A. and Edwards, J. R., ***Large-Eddy Simulation / Reynolds-Averaged Navier-Stokes Simulations of High-Speed Mixing Processes***, AIAA J., 52(7):1486–1501 (2014).

[39] Wilcox, D. C., ***Formulation of the*** $\mathrm{k}-\omega$ ***Turbulence Model Revisited***, AIAA J., 46(11):2823–2838 (2008).

[40] Rumsey, C. L. and Gatski, T. B., ***Summary of EASM Turbulence Models in CFL3D with Validation Test Cases***, NASA/TM 2003-212431, NASA Langley Research Center, Hampton, VA (Jun. 2003).